Assessing the Role of Air–Sea Coupling in Predicting Madden–Julian Oscillation with an Atmosphere–Ocean Coupled Model

JIYE WU,[a] YUE LI,[a] JING-JIA LUO,[a] AND XIANAN JIANG[b]

[a] *Institute of Climate Application Research, Collaborative Innovation Center on Forecast and Evaluation of Meteorological Disasters, Key Laboratory of Meteorological Disaster of Ministry of Education, Nanjing University of Information Science and Technology, Nanjing, China*

[b] *Joint Institute for Regional Earth System Science and Engineering, University of California, Los Angeles, Los Angeles, California*

(Manuscript received 23 December 2020, in final form 8 August 2021)

ABSTRACT: The Madden–Julian oscillation (MJO) provides an important source of subseasonal-to-seasonal (S2S) predictability. Improved MJO prediction can be beneficial to S2S prediction of global climate and associated weather extremes. In this study, hindcasts based on an atmosphere–ocean coupled general circulation model (CGCM) are compared to those based on atmosphere general circulation models (AGCMs) to investigate influences of air–sea interactions on MJO prediction. Our results suggest that MJO prediction skill can be extended about 1 week longer in the CGCM hindcasts than AGCM-only experiments, particularly for boreal winter predictions. Further analysis suggests that improved MJO prediction in the CGCM is closely associated with improved representation of moistening processes. Compared to the AGCM experiments, the CGCM better predicts the boundary layer moisture preconditioning to the east of MJO convection, which is generally considered crucial for triggering MJO deep convection. Meanwhile, the widely extended east–west asymmetric structure in free-tropospheric moisture tendency anomalies relative to the MJO convection center as seen in the observations is also well predicted in the CGCM. Improved prediction of MJO moisture processes in CGCM is closely associated with better representation of the zonal scale of MJO circulation and stronger Kelvin waves to the east of MJO convection, both of which have been recently suggested to be conducive to MJO eastward propagation. The above improvements by including air–sea coupling could be largely attributed to the realistic MJO-induced SST fluctuations through the convection–SST feedback. This study confirms a critical role of atmosphere–ocean coupling for the improvement of MJO prediction.

KEYWORDS: Madden-Julian oscillation; Climate prediction; Forecast verification/skill; Hindcasts; Intraseasonal variability

1. Introduction

It is well known that weather forecasting (i.e., the forecast of weather regimes from a few hours up to about 2 weeks) and climate prediction have been remarkably improved over the last decades. However, the extended-range forecast as the gap between the weather forecast and climate prediction is still far from satisfactory. It remains a great challenge to fill this gap in order to perform a reliable, skillful, and seamless forecast of the weather–climate continuum (e.g., Palmer et al. 2008; Merryfield et al. 2020). Recently, subseasonal prediction, as the bridge to fill this gap, has gained more and more attention. To improve the operational predictions and social applications, the Subseasonal to Seasonal (S2S) Prediction research project has been launched by the World Weather Research Programme/World Climate Research Programme (Vitart et al. 2017) toward the development of weather-to-climate seamless forecasts.

The Madden–Julian oscillation (MJO), which is recognized as one of the primary sources of subseasonal prediction, has been intensively studied (e.g., Waliser et al. 2003; Zhang 2005, 2013; Zhang et al. 2020; Pegion and Sardeshmukh 2011; Jiang et al. 2020a). The MJO is a dominant mode of subseasonal variability in the tropics with a period of 30–60 days and characterized as an eastward propagation of large-scale convective features with a speed of ~5 m s^{-1} (e.g., Madden and Julian 1971, 1972). Given its tremendous influences on global climate and weather systems (e.g., Cassou 2008; Stan et al. 2017), many climate prediction centers have been dedicated to improving the prediction of MJO. In recent decades, MJO prediction has been improved with the advances of theoretical understanding, observations, model development, and computing technology. Most models' hindcasts participating in the S2S project show a good MJO prediction skill at lead times of up to about 20 days, among which the multimember ensemble mean of ECMWF model can even skillfully predict MJO approximately 30 days in advance (e.g., Vitart 2017; Lim et al. 2018). However, considering the intrinsic potential MJO predictability of 4–6 weeks as suggested by recent studies (e.g., Neena et al. 2014; Kim et al. 2018), there is still room for improvement of MJO prediction skill.

The MJO prediction skill can be affected by a variety of factors, including biases in model physics, the initialization scheme, the phase and amplitude of the MJO (e.g., Lin et al. 2008; Rashid et al. 2011; Fu et al. 2011; Liu et al. 2017; Kim et al. 2018). For instance, Wang et al. (2014) showed that MJO prediction skill at a longer lead time is relatively higher during target phases 3 and 7, whereas it becomes lower during target phases 8, 1, and 2. In addition, MJO prediction skill largely depends on the season and MJO amplitude in most of operational forecast systems. For instance, it is shown that the

Corresponding author: Jing-Jia Luo, jingjia_luo@hotmail.com; jjluo@nuist.edu.cn

DOI: 10.1175/JCLI-D-20-0989.1

prediction skill is higher in boreal winter than that in summer (e.g., Wang et al. 2014), and when strong MJO events are present in the model initial condition (e.g., Lin et al. 2008; Wang et al. 2014; Xiang et al. 2015). In addition, the behavior and prediction of the MJO are also modulated by air–sea interactions (Fu et al. 2013; Shelly et al. 2014; Green et al. 2017; Kim et al. 2018), atmosphere mean states (DeMott et al. 2015; Gonzalez and Jiang 2017; Kim 2017; Lim et al. 2018), and seasonal–interannual climate variability such as the Indian Ocean dipole (IOD; Liu et al. 2017), El Niño–Southern Oscillation (ENSO; Wang et al. 2017a; Wei and Ren 2019), and quasibiennial oscillation (QBO; Marshall et al. 2017; Son et al. 2017; Lim et al. 2019). However, some debates still exist with regard to the significance of the modulation by these climate modes (Liu et al. 2017; Kim et al. 2019).

Recent studies have emphasized the importance of complex feedbacks between the atmosphere and ocean in affecting the MJO (e.g., DeMott et al. 2015; Jiang et al. 2020a). For instance, convection and wind anomalies related to the MJO could induce anomalous solar radiation, evaporative cooling, and momentum flux that influence the upper ocean. The generated ocean surface perturbations in turn can force the atmosphere. Some studies have shown that the effect of direct heat flux forcing caused by SST anomalies is very limited (DeMott et al. 2016). In contrast, several indirect feedbacks from the upper ocean may play active roles in regulating MJO activity (e.g., Wang and Xie 1998; Marshall et al. 2008; Liu and Wang 2013; DeMott et al. 2015, 2016, 2019). For instance, the air–sea interaction is considered to have a role in maintaining the MJO over the warm pool by destabilizing atmospheric moist Kelvin wave (e.g., Wang and Xie 1998). From the perspective of evaporation–wind feedback, Marshall et al. (2008) proposed a mechanism emphasizing the role of SST-driven evaporation and moisture convergence related to increased shortwave radiation over the eastern flank of MJO convection. Recent studies showed that ocean feedbacks can increase horizontal moisture advection and moisture convergence and hence favor the eastward propagation of MJO convection (e.g., Hsu and Li 2012; DeMott et al. 2019).

However, there is still no consensus about the influence of atmosphere–ocean coupling on MJO prediction in dynamical models. Several studies demonstrated that the atmosphere general circulation model (AGCM) forced with high-temporal-resolution SST has better performance in forecasting MJO compared to that forced with low-temporal-resolution SST (e.g., Kim et al. 2008), and similar preponderance is also found in a coupled GCM compared to the AGCM (e.g., Seo et al. 2009; Kim et al. 2010, 2018; Fu et al. 2013; Shelly et al. 2014; Green et al. 2017). However, Klingaman and Woolnough (2014) pointed out that the sensitivity of MJO simulation to air–sea feedbacks might be overlaid by mean-state bias between the coupled and the uncoupled models. Fu et al. (2015) also argued that the influence of atmosphere–ocean interactions on MJO prediction varies from event to event.

In summary, although it has been emphasized in several previous studies, the role of the ocean in predicting the MJO is not yet clearly understood. Since the ocean interacts with the MJO on various time scales, the impacts of low-frequency ocean variability were not fully discussed. In addition, the exact role of atmosphere–ocean coupling might be model dependent, so results using different models are beneficial for reaching a consensus. In this study, we assessed the importance of air–sea coupling based on a global coupled model: the Scale Interaction Experiment–Frontier Research Center for Global Change (SINTEX-F; Luo et al. 2003). Previous studies have shown that this model has a good performance in simulating tropical climate and reducing equatorial SST biases with an improved coupling physics (Luo et al. 2003, 2005b). This model can well predict tropical climate variations such as ENSO and IOD on seasonal-to-multiyear time scales (Luo et al. 2005a, 2007, 2008a,b; He et al. 2020). The initial conditions of the SINTEX-F prediction system were generated by a simple coupled SST-nudging scheme and hence do not contain the MJO information.

In this study, we further assimilate the JRA-25 6-hourly data into the model in order to obtain realistic atmosphere information in the initial conditions. By performing a set of 2-month hindcast experiments with and without air–sea coupling, we explored the influence of air–sea interactions on MJO prediction. Section 2 describes details of the forecast system, experiment designs, analysis methods, and observational data used for validation. Then a general assessment of model performance in predicting tropical circulation and convection related to the MJO is conducted in section 3. Section 4 compares MJO forecast skills in coupled and AGCM-only experiments. Section 5 illustrates the effects of the atmosphere–ocean interactions on the prediction of MJO evolution. The results are summarized and discussed in section 6.

2. Model hindcast experiments and methodology

a. Model and experiments

In this study, one coupled and two AGCM-only hindcast experiments (Table 1) have been carried out to examine the role of air–sea coupling in predicting the MJO. The coupled general circulation model (CGCM) experiment is conducted using the globally coupled SINTEX-F model. Its atmospheric component is ECHAM4 with a horizontal resolution of $1.1° \times 1.1°$. It uses a 19-level hybrid sigma–pressure vertical coordinate with model top at 10 hPa (Roeckner et al. 1996). The physical processes used in the model include the bulk mass flux formula of Tiedtke (1989) for cumulus convection and the code of Morcrette et al. (1986) for radiation [see Luo et al. (2005b) for more detailed descriptions]. The oceanic component is the OPA 8.2 (Madec et al. 1998) with the ORCA2 configuration: an Arakawa-C type grid based on a 2° Mercator mesh. In the Northern Hemisphere, the Arctic pole is transformed to two poles in the Eurasian and North American continent, respectively, and the anisotropy ratio of the grid meshes after the transformation becomes nearly one everywhere. The OPA model resolution is 2° cos(latitude) in latitude $\times$ 2° in longitude with finer meridional resolutions of 0.5° near the equator to better simulate the equatorial waves. There are 31 vertical z levels of which 19 levels lie at the top 400 m. The coupling fields are exchanged every 2 h between the ocean and atmosphere

TABLE 1. Three hindcast experiments (1984–2008). We have performed 300 runs (i.e., 25 yr × 12 months yr^{-1}) for each experiment, and each run is integrated for 2 months.

Expt	Model	SST forcing	Initialization
CTL	AGCM (ECHAM 4.6)	Climatological SST	Nudging 6 hourly u wind, v wind, air temperature, surface pressure of JRA-25 and SST of OISST v2
AMIP	AGCM (ECHAM 4.6)	Observed SST	
CGCM	CGCM (SINTEX-F, ECHAM 4.6 + OPA 8.2)	Predicted SST in the coupled model	

without any flux correction by the Ocean Atmosphere Sea Ice Soil (OASIS) 2.4 coupler (Valcke et al. 2000). Impacts of the ocean surface currents on the surface momentum flux have been considered (Luo et al. 2005b). Detailed descriptions of the model are given to Luo et al. (2005a,b).

In addition to the coupled model experiment, two complementary AGCM-only hindcasts using ECHAM4 model are conducted, namely, the control experiment (CTL) and the AMIP experiment. To completely remove the influence of upper-ocean variability, the CTL experiment is persistently forced by the observed climatological monthly mean SST. In the AMIP experiment, the atmosphere is forced by the observed monthly SST, derived from the NOAA SST reanalysis blended from in situ data and infrared satellite data using optimum interpolation (OISST v2; Reynolds et al. 2002). Note that the prescribed monthly SST data in both the CTL and AMIP experiments are linearly interpolated to obtain SST fields at each model time step.

All the three experiments are initialized from the first day of each month from January 1984 to December 2008 and then integrated for 2 months (about 60 days), so we have performed 25 years × 12 months = 300 runs for each experiment. The initial conditions for ECHAM4 are obtained from a simple spectral nudging scheme that assimilates the 6-hourly u wind, v wind, air temperature, and surface air pressure derived from the JRA-25 reanalysis data (Onogi et al. 2007). The spectral nudging coefficients of divergence, vorticity, air temperature, and surface air pressure are 0.579 (48 h), 4.63 (6 h), 1.16 (24 h), and 1.16 (24 h), respectively (Jeuken et al. 1996). In addition to the realistic atmospheric forcing, the model SST in the CGCM is also strongly nudged toward the observed SST interpolated from NOAA weekly OISST v2 data (i.e., the coupled SST–nudging initialization scheme; see Luo et al. 2005a). This simple coupled data assimilation scheme helps reduce the model's initial shock and improve climate prediction skill (e.g., Luo et al. 2005a, 2008a,b).

Figure 1 displays the anomaly correlations between the observation (see section 2b) and the initial conditions generated by the spectral nudging scheme. We examined the initial conditions of anomalous outgoing longwave radiation (OLR) and zonal wind at pressure levels of 850 hPa (U850) and 200 hPa (U200) that are used for calculating the MJO metrics. Significantly high correlations (>0.90) are found for zonal winds at both 200 and 850 hPa over most regions of the globe (Figs. 1a,b). Relatively low correlations of the U850 are found over the Tibetan Plateau, the eastern coast of Africa, and the west coasts of North and South America, where the topography is dominated by high mountains. In contrast, much lower correlations are found in OLR between the model initial conditions and the NOAA satellite observations, particularly over the tropical region (Fig. 1c). Similar correlations in OLR can be obtained if compared against the OLR from the JRA-25 instead of NOAA OLR. This is probably due to the fact that the model OLR is derived based on cloud and convection parameterizations, in which large uncertainty can be involved. Assimilating moisture observations might help improve the OLR initial conditions (Wu et al. 2020), which warrants a future study.

b. Validation data

The observational daily data used in this study during 1984–2008 includes zonal winds, meridional winds, vertical velocity, air temperature, geopotential height, and specific humidity from JRA-25 datasets (Onogi et al. 2007), OLR from the National Oceanic and Atmospheric Administration (NOAA; Liebmann and Smith 1996), and observed SST data provided by AVHRR-OISST v2 (Reynolds et al. 2007).

c. Calculation of the MJO indices

The Real-Time Multivariate MJO (RMM) index (Wheeler and Hendon 2004, hereafter WH04) has been widely used to detect coupled MJO signals between deep convection and circulation along the equatorial zone. The averaged U850, U200, and OLR between 15°S and 15°N are used for a combined empirical orthogonal function (EOF) analysis. The RMM1 and RMM2 are defined as the PC1 and PC2 of the first two leading EOF modes. The RMM indices can represent the amplitude of MJO, and the phase angle derived from the RMMs can capture its propagation feature. The calculation of the observed and forecasted MJO indices follows the procedures described in previous studies (e.g., Lin et al. 2008; Gottschalck et al. 2010; Rashid et al. 2011; Vitart 2017), and the removal of the 120-day running mean is used to subtract interannual variability. Due to the short integration (i.e., 2 months) of each forecast, the reanalysis data are concatenated preceding the model initial date to compute the 120-day running mean.

Following Wang et al. (2014), each variable associated with the RMM index is denoted as $X(t, \tau)$, where t represents the initial time and τ represents the lead days. The intraseasonal anomalies of each 2-month forecast are obtained by the following steps:

1) The daily climatology is calculated from the mean of the forecasts during 1984–2008 as a function of lead day and start calendar month.
2) The raw daily anomaly $A(t, \tau)$ is calculated by subtracting the daily climatology from $X(t, \tau)$.
3) Previous 120-day averages are removed on each grid. Assuming the forecast target day is n, we compute the

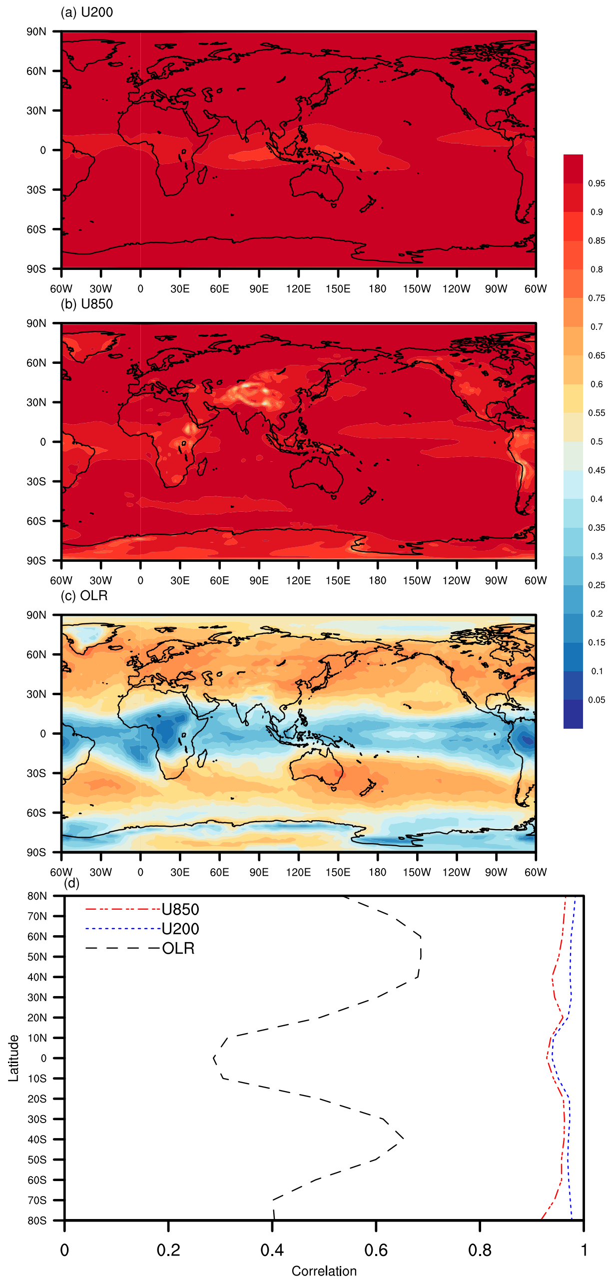

FIG. 1. Correlation coefficients between the observations and initial conditions of (a) U200, (b) U850, and (c) OLR anomalies during 1984–2008. (d) Zonal mean of the correlations as a function of latitude. Note that the observed OLR is derived from the NOAA satellite observation and results based on the JRA-25 OLR are similar.

running mean of the forecast anomalies at lead times of $1-n$ days and the observational anomaly $O(t)$ of $120-n$ days prior to the model initial date: $A_m(t,\ \tau) = (1/120)\left[\sum_{i=1}^{n} A(t,\ i) + \sum_{i=1}^{120-n} O(t-i)\right]$, and then we subtract this 120-day mean anomaly from the daily anomaly to get rid of the interannual variability: $A_s(t,\tau) = A(t,\tau) - A_m(t,\tau)$.

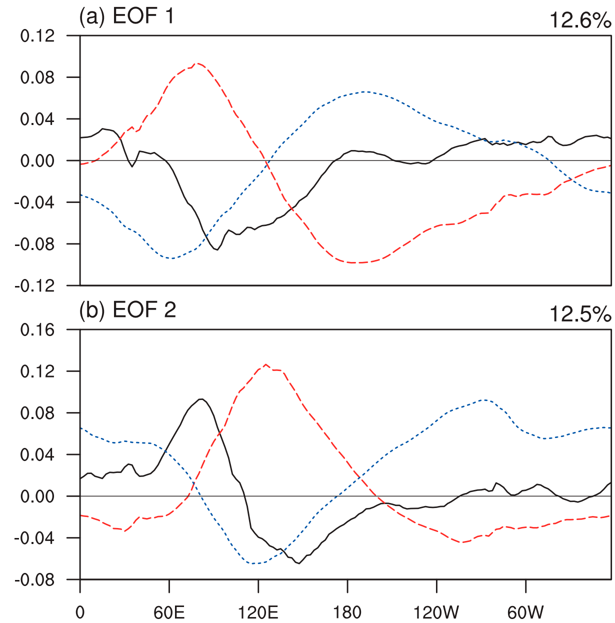

FIG. 2. The (a) first and (b) second leading EOF eigenvectors of combined fields of OLR (black solid lines), U850 (red dashed lines), and U200 (blue dotted lines). The variance explained by each mode is given at the top right of each panel.

The observed RMMs are obtained from the PCs of the first two leading combined EOF modes of OLR, U850, and U200 anomalies, while the forecast RMMs are reconstructed by projecting the forecast anomalies of OLR, U850, and U200 onto the observed two EOFs modes (Fig. 2). Note that the anomaly of each variable has been normalized by its standard deviation based on the observations, following Gottschalck et al. (2010). In this study, the wind fields derived from JRA-25 datasets are used for validation, which slightly differs from the NCEP reanalysis datasets used in WH04. Thus, the observed RMMs are derived based on the multivariate EOF analysis using OLR from NOAA and zonal winds from JRA-25 (Fig. 2). Similar to what is shown in Fig. 1 of WH04, EOF1 characterizes enhanced convection over the eastern Indian Ocean and Maritime Continent, and EOF2 depicts enhanced convection over the western Pacific (WP) and suppressed convection over the tropical Indian Ocean (TIO). In addition, A spatial phase shift between convection and zonal winds, along with a baroclinic structure of circulation in the upper and lower troposphere can be found as in WH04.

Apart from the RMMs, we also calculated intraseasonal anomalies of several fields related to the MJO diagnoses (see section 5) by subtracting the 120-day running mean and then applying an additional 5-day running mean to smooth out the high-frequency signal.

d. *Measure of MJO prediction skill*

The anomaly correlation coefficient (ACC) and root-mean square error (RMSE) are often used to quantify prediction skill. In this study, the bivariate ACC and RMSE as a function of lead time based on the observed and predicted RMM1 and

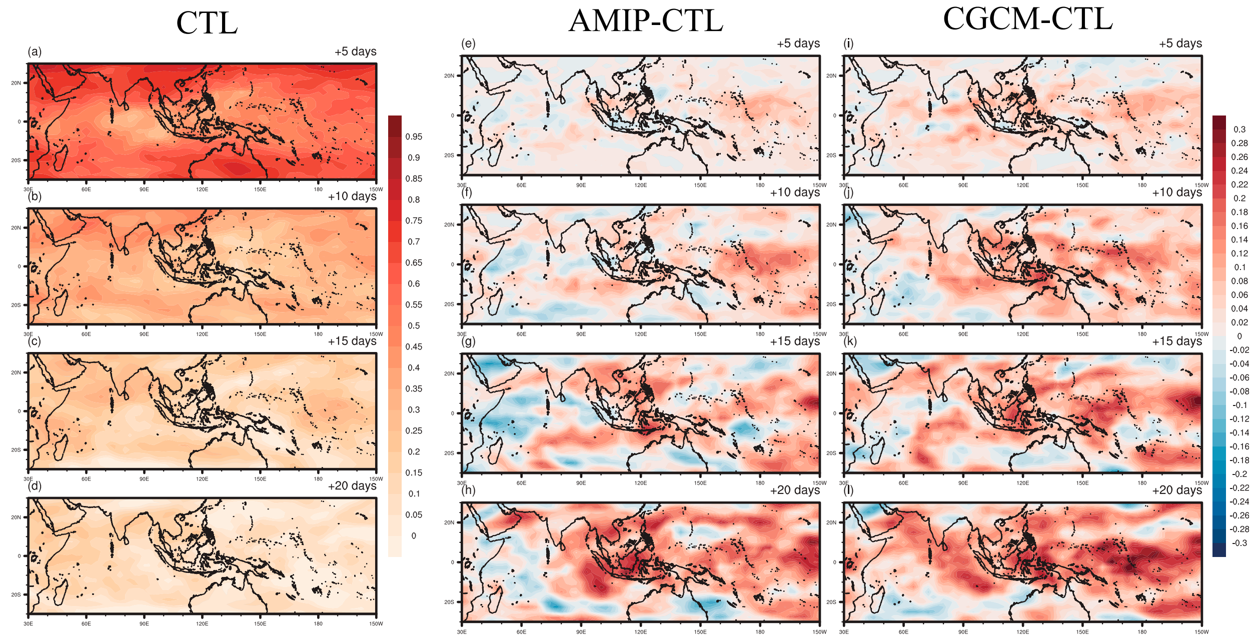

FIG. 3. (a)–(d) Anomaly correlation coefficient (ACC) scores between the predicted and observed U200 at the lead time of (top to bottom) +5, +10, +15, and +20 days over the region of 30°N–30°S, 30°E–180° during the period 1984–2008 in the CTL, as well as (e)–(h) their difference between the AMIP and the CTL and (i)–(l) their difference between the CGCM and the CTL.

RMM2 are computed to represent MJO prediction skill, which are shown as follows (Lin et al. 2008; Rashid et al. 2011):

$$\mathrm{ACC}(\tau) = \frac{\sum_{t=1}^{n}[a_1(t)b_1(t_0,\tau) + a_2(t)b_2(t_0,\tau)]}{\sqrt{\sum_{t=1}^{n}[a_1^2(t) + a_2^2(t)]}\sqrt{\sum_{t=1}^{n}[b_1^2(t_0,\tau) + b_2^2(t_0,\tau)]}},$$

$$\mathrm{RMSE}(\tau) = \sqrt{\frac{1}{n}\sum_{i=1}^{n}\{[a_1(t) - b_1(t_0,\tau)^2] + [a_2(t) - b_2(t_0,\tau)^2]\}},$$

where $a_1(t)$ and $a_2(t)$ are the observed RMM1 and RMM2 at day t, and $b_1(t_0, \tau)$ and $b_2(t_0, \tau)$ represent their corresponding forecasts from time t_0 with a lead time of τ days. The baselines for ACC and RMSE as useful prediction skill are 0.5 and $\sqrt{2}$, respectively. The latter is because the standard deviation of observed RMMs is about 1, so that the bivariate root-mean-square error is about $\sqrt{2}$ (Rashid et al. 2011).

3. Overall prediction skill of atmospheric circulation and convection

In this section, we first evaluated the overall prediction skill of the zonal wind anomalies in the upper and lower troposphere based on the three hindcast experiments. Figure 3 shows the ACC between the observed and predicted U200 at lead times of 5, 10, 15, and 20 days in the CTL and its difference from the other two sets of experiments. In general, the forecasts at the lead time of 5 days show significantly high correlations ($r > 0.8$) in the CTL (Fig. 2a), although relatively low correlations are found in the equatorial central-eastern Indian Ocean ($r > 0.3$) and western Pacific Ocean ($r > 0.6$) where the MJO is active. The correlations decrease with the increasing forecast lead time, and in most of the tropical regions the skill is still positive at 20 days lead (Fig. 3d).

It is shown that the differences in the correlations between the AMIP and the CTL (AMIP-CTL; middle column in Fig. 3) remain positive over the tropical Indian-Pacific region for predictions at all of the four lead times, indicating a generally higher prediction skill when the AGCM is forced by observed monthly SST. The differences of the correlations become larger with the increasing lead time, which reaches approximately 0.3 over the tropical eastern Indian Ocean and Pacific at a lead time of 20 days (Fig. 3h). Similarly, the correlation difference between the CGCM and the CTL (CGCM-CTL; right column in Fig. 3) remains positive at lead times of up to 20 days. In addition, positive differences between the CGCM and the AMIP can also be seen in parts of the tropics, which may indicate the possible contributions of air–sea interactions since the SST values in the CGCM forecasts are close to but not identical to the observed values in the AMIP experiment. Please note that these anomalous fields contain the total variations from synoptic to interdecadal time scale. Skill related to the MJO is discussed in section 4.

Similar results are also found in the predictions of the tropical U850 anomalies (not shown). Although the correlation skill in predicting the OLR is lower compared to the zonal wind anomalies (not shown), the AMIP and CGCM experiments also show improved prediction skills compared to the CTL. The lower prediction skills of the OLR can be attributed to the low ACC between the OLR initial conditions and the observations (recall Fig. 1c).

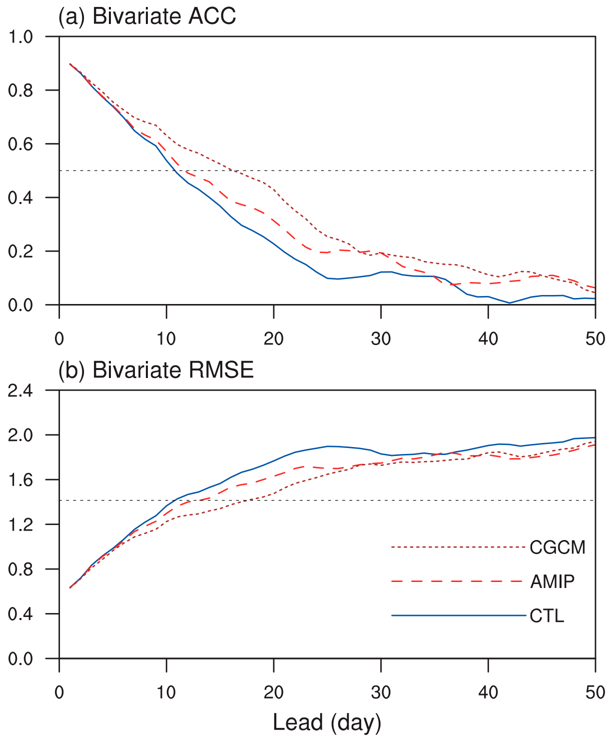

FIG. 4. (a) ACC and (b) RMSE skill in predicting the RMM indices as a function of lead time, based on the CTL, AMIP, and CGCM hindcast experiments during 1984–2008. The horizontal dashed line in each panel indicates the baseline of useful skill (i.e., ACC = 0.5 and RMSE = $\sqrt{2}$).

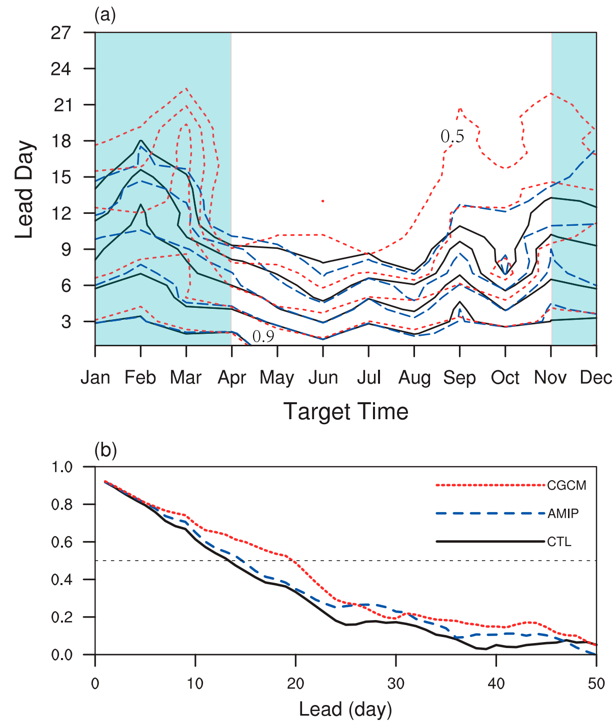

FIG. 5. (a) Bivariate ACC of the RMM1 and RMM2 as a function of start month and lead time based on the three hindcast experiments. The contours are plotted from 0.5 (top line) to 0.9 (bottom line) with an interval of 0.1. (b) As in Fig. 4a, but for skill comparison based on the winter season [November–April; see the blue shading in (a)].

4. MJO prediction skills

In this section, we examine MJO prediction skill based on the RMM indices in three experiments. The eastward movement is a key characteristic though the MJO shows complex propagation features in boreal summer (Lawrence and Webster 2002; Jiang et al. 2004). Figure 4 displays prediction skill for the RMM indices during the entire year for an overall assessment of MJO skill, which is about 12, 13, and 18 days in the CTL, AMIP, and CGCM experiments, respectively, corresponding to ACC (RMSE) skill of 0.5 ($\sqrt{2}$). This result suggests that including the air–sea coupling in CGCM can significantly improve MJO prediction skill by almost 1 week over the two sets of AGCM-only forecasts (Fig. 4).

Considering its pronounced seasonality in propagation characteristics (e.g., Wang and Xie 1996; Jiang et al. 2018), MJO forecast skill can be different in summer and winter. Previous studies showed that the ACC skill of the MJO prediction is usually higher during boreal winter than that in summer (e.g., Lin et al. 2008; Wang et al. 2014). We further examined the variation of the ACC skill among the 12 calendar months (Fig. 5a). Our results show that the ACC skill is substantially higher during boreal winter (November–April) than during boreal summer (May–October) across all the three hindcast experiments, in agreement with previous studies. Interestingly, the prediction skills are largely improved during September to March in the CGCM experiment, suggesting that the tropical atmosphere–ocean interactions have a strong influence on the MJO in these months. By averaging the bivariate ACC of the RMM indices during boreal winter, the useful prediction skill increases to approximately 14 (CTL), 15 (AMIP), and 20 (CGCM) lead days, respectively. Compared to ACC skill in predicting the intraseasonal variations throughout the entire year, the lead time with useful forecast is 2–3 days longer during the boreal winter in all the three experiments (Figs. 4a and 5b).

To further evaluate the influence of air–sea coupling on prediction of large-scale convection and circulation related to the MJO, we also compared prediction skill of the RMM indices-constructed OLR, U850, and U200, respectively (hereafter referred as RMM_OLR, RMM_U850, and RMM_U200), following Kim et al. (2014). They are obtained by projecting the observed and predicted anomalies of each variable onto the corresponding component of the two leading combined EOF eigenvectors described above.

The ACC skills of the RMM_OLR, RMM_U850, and RMM_U200 as a function of lead time are shown in Fig. 6. The impacts of the atmosphere–ocean interactions on the prediction of the MJO-related zonal wind and convection are found to be similar to their impacts on the prediction of the total RMM indices (recall Figs. 4 and 5). The prediction skills by the CGCM experiment are higher than that in the CTL and AMIP hindcast experiments. The advantage of the coupled model is found to be more obvious for the RMM_OLR (Fig. 6a),

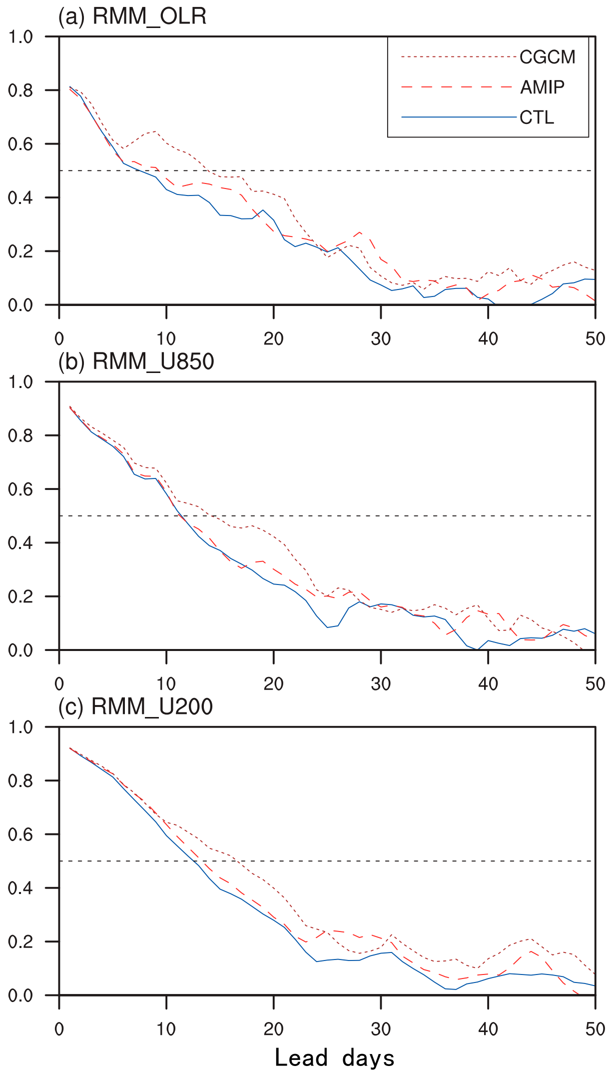

FIG. 6. Bivariate ACC skill of the RMM indices constructed with (a) OLR, (b) U850, and (c) U200 respectively based on the CTL, AMIP, and CGCM hindcast experiments during boreal winter (November–April) in 1984–2008.

especially during the second and third forecast week (i.e., at 8–21-day lead), indicating a more critical role of the atmosphere–ocean coupling in predicting the MJO-related convection compared to the MJO-related circulation. Interestingly, the ACC of the RMM_OLR at 1-day lead reaches about 0.8, while the tropical OLR on each grid is poorly reproduced in the initial conditions (recall Fig. 1c). This discrepancy may occur because the RMM_OLR mostly reflects the large-scale MJO activities that can be better reproduced in the model.

5. Prediction of MJO evolution

a. Diagnostics of MJO propagation

The aforementioned results indicate that the atmosphere–ocean coupling plays an important role in improving the MJO forecast. In this section, we attempt to explore how the air–sea coupling influences the MJO prediction. The roles of air–sea interactions in the prediction of MJO events over the periods of observational campaigns such as the Tropical Ocean Global Atmosphere—Coupled Ocean–Atmosphere Response Experiment (TOGA COARE), Year of Tropical Convection (YOTC), and Dynamics of the MJO/Cooperative Indian Ocean Experiment on Intraseasonal Variability in the Year 2011 (DYNAMO/CINDY) experiments were discussed in a variety of previous studies (e.g., Woolnough et al. 2007; Shelly et al. 2014; Fu et al. 2013). In this section, a suite of diagnoses are applied to the hindcasts with a longer period (i.e., 1984–2008).

The role of air–sea interactions for MJO development and propagation is analyzed by comparing the temporal-spatial evolution of intraseasonal convections in the observations and the three sets of hindcast experiments. Following Jiang (2017), the observed and predicted MJO evolution patterns are derived by lead–lag regression of OLR anomaly onto itself averaged over the equatorial eastern Indian Ocean (EEIO; 5°N–5°S, 75°–85°E). Note that the regression coefficients are scaled by −1 standard deviation (STD) of the EEIO OLR anomalies for the sake of convenience. Given that the hindcasts in this study are initialized once per month, we choose different days in each month, rather than one specific day, as the reference time to conduct lead–lag regression to make the results more reliable. Table 2 shows pattern correlation coefficients (PCCs) between

TABLE 2. Pattern correlation coefficients (PCC) between the observed and predicted time–longitude evolution of the regressed OLR anomalies averaged over 10°N–10°S in the three sets of hindcast experiments based on the regressions against the EEIO OLR at different reference times (i.e., the 1st, 2nd, . . . , 21th day of each month). PCC is calculated on a time–longitude domain of 40°E–180° and lead times of +1 to +31 days.

Reference time (the *N*th day of each month)	CTL	AMIP	CGCM
1	0.77	0.83	0.87
2	0.82	0.87	0.90
3	0.83	0.87	0.90
4	0.82	0.84	0.90
5	0.80	0.81	0.88
6	0.79	0.78	0.87
7	0.78	0.76	0.88
8	0.78	0.76	0.88
9	0.81	0.79	0.89
10	0.83	0.82	0.89
11	0.83	0.82	0.90
12	0.82	0.83	0.92
13	0.82	0.84	0.93
14	0.84	0.84	0.93
15	0.85	0.84	0.93
16	0.86	0.84	0.93
17	0.87	0.86	0.92
18	0.87	0.86	0.91
19	0.87	0.84	0.90
20	0.87	0.84	0.89
21	0.87	0.84	0.89

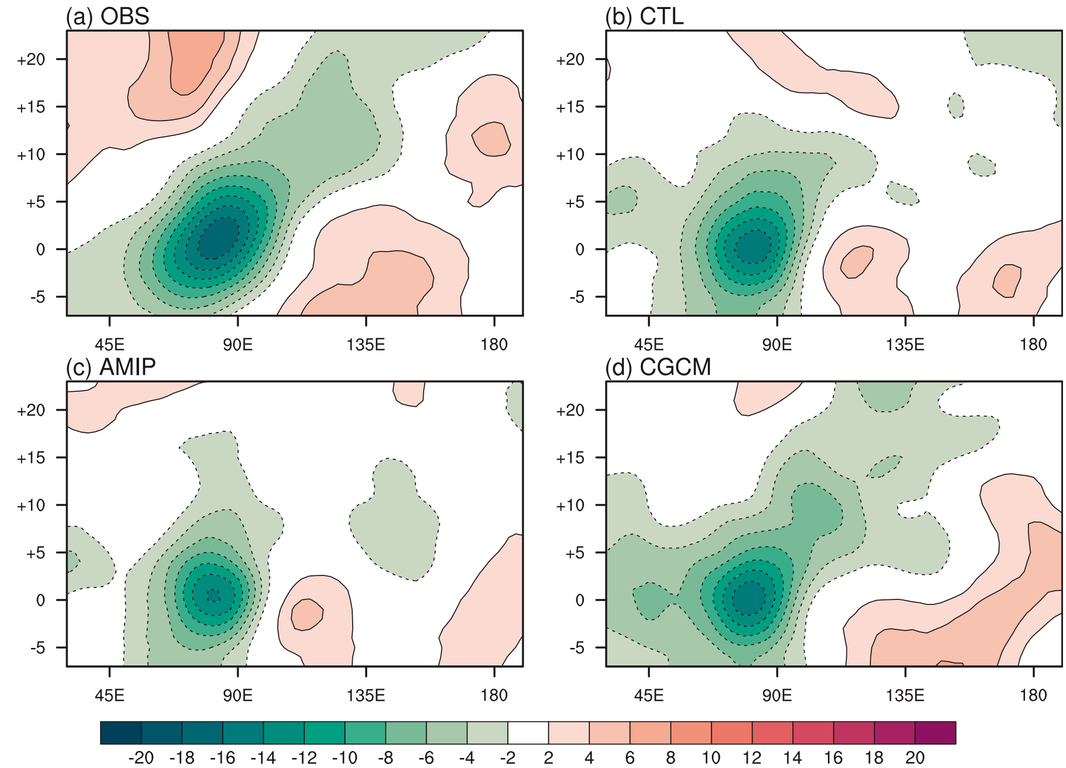

FIG. 7. Longitude–time diagram of regressed intraseasonal OLR anomalies (units: W m^{-2}) along the equator (10°N–10°S average) in (a) observations and (b)–(d) three sets of hindcast experiments based on the lead–lag regressions of anomalous OLR onto itself averaged over the equatorial eastern Indian Ocean (EEIO; 5°N–5°S,75°–85°E) on the eighth day of each month. All the regressed patterns in the observation and predictions are scaled by -1 standard deviation (STD) of the OLR anomalies averaged over the EEIO. The *y* axis denotes the lag days from the reference time (i.e., the eighth day of each month).

the observed and predicted MJO evolutions of patterns on the Indo-Pacific regions (40°E–180°). The PCC scores in the CGCM are consistently higher than that in the two AGCM-only hindcasts (Table 2), which suggests improved prediction of MJO evolutions in the coupled model. Considering the difference of the prediction skill between the AGCM-only and CGCM hindcasts becomes clearer 1 week after the initial forecast date (recall Figs. 4 and 5), the following diagnoses focus on the results when the reference time is the eighth day of each month (hereafter RTD8). In addition, this regressed pattern can better represent an entire evolution of MJO convection during days 1–31 for the MJO events that start to occur on day 1 (i.e., the first day of each month).

Figure 7 shows Hovmöller diagrams of the lead–lag regressed OLR anomalies along the equator relative to RTD8. The observed MJO evolution pattern shows a systematic eastward propagation from the Indian Ocean to the western Pacific (Fig. 7a). Compared to the observation, the eastward-propagating signal is relatively weaker in the CTL and AMIP hindcast experiments (Figs. 7b,c), while largely captured in the CGCM hindcasts (Fig. 7d), again suggesting the importance of air–sea coupling. We further examine the temporal evolution of the MJO-related convection and circulation based on the regressed OLR and 850-hPa wind anomalies from lag -5 to lag $+15$ (Fig. 8). Note that all the following regressed patterns were scaled by -1 STD of EEIO OLR anomalies. Consistent with the results depicted in Fig. 7, the MJO convection in the AGCM-only experiments (i.e., the CTL and AMIP) can be initialized and intensified over the TIO only at lead times of up to 2 weeks (around lag $+5$), but the signal fails to propagate across the Maritime Continent (MC) in the following days. In contrast, this shortcoming in the model prediction can be partly reduced by coupling an ocean model (the right column of Fig. 8). With the development and eastward propagation of MJO convection, a Gill–Matsuno type of response (Matsuno 1966; Gill 1980) is induced by the convective heating in the observation and predictions: namely, anomalous easterly (westerly) occurs to the east (west) of the convection in the lower troposphere.

b. *Physical processes underpinning the MJO propagation*

To investigate possible underlying mechanisms underpinning the influence of air–sea interactions on the prediction of MJO evolution, we diagnosed several physical processes associated with MJO propagation. According to the moisture mode theory (Adames and Maloney 2021), MJO convection is tightly coupled to column-integrated moist static energy

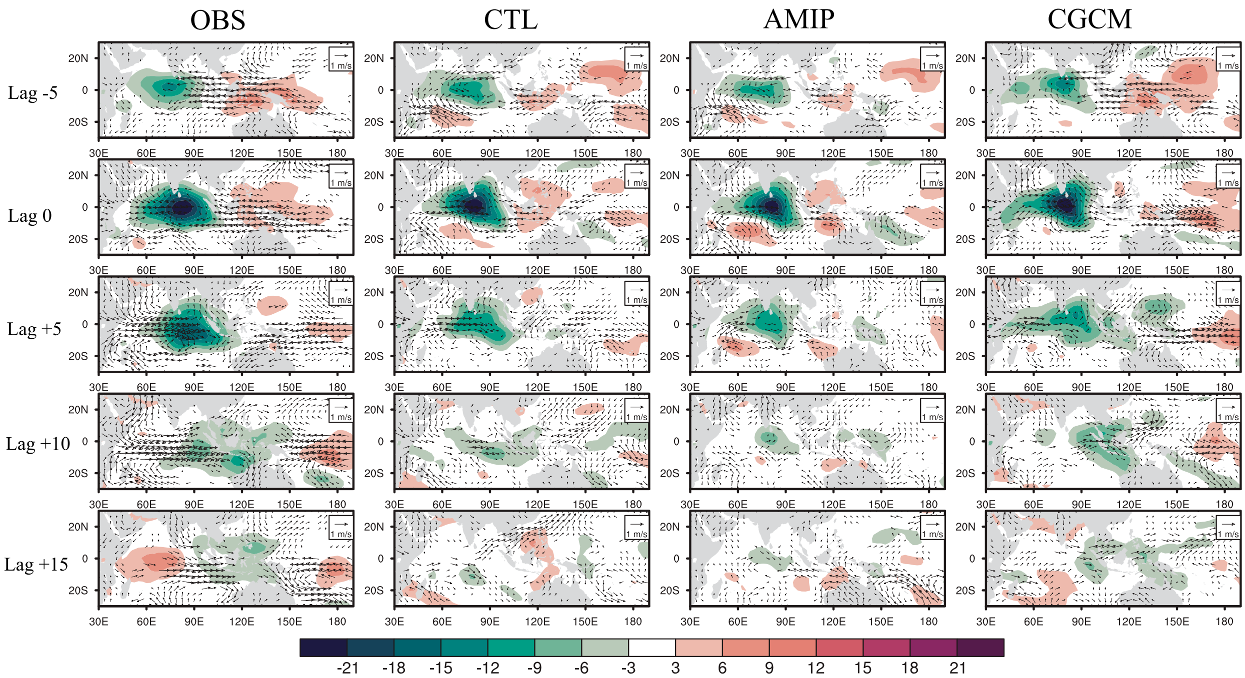

FIG. 8. Regressed intraseasonal anomalies of OLR (shaded; W m^{-2}) and 850-hPa wind (vectors; m s^{-1}) (top to bottom) from lag −5 to lag +15 based on lead–lag regression against the EEIO OLR anomaly at the eighth day of each month in (left) observation and (remaining columns) three sets of hindcasts. Wind fields are only plotted when u wind speed is greater than 0.9 m s^{-1} and v wind speed is greater than 0.1 m s^{-1}. Spatial smoothing is performed by nine-grid running average.

(MSE). A zonal asymmetry of column MSE tendency, positive to the east of convection and negative to the west of convection, is considered critical for MJO eastward propagation (e.g., Maloney 2009; Jiang 2017; Wang et al. 2017b). The MSE is defined as

$$m = c_p T + gz + Lq, \tag{1}$$

where T is temperature, c_p is specific heat at constant pressure (1004 J K^{-1} kg^{-1}), z is geopotential height, g is gravitational acceleration (9.8 m s^{-2}), q is specific humidity, and L is latent heat of vaporization at 0°C.

And the corresponding vertically column-integrated MSE tendency formula can then be written as follows:

$$\left\langle \frac{\partial m}{\partial t} \right\rangle = -\langle \mathbf{V} \cdot \nabla m \rangle - \left\langle \omega \frac{\partial m}{\partial p} \right\rangle + Q_r + Q_t, \tag{2}$$

where $\mathbf{V}$ denotes the horizontal velocity, ω is pressure vertical velocity, and angle brackets represent a mass-weighted vertical integral from 1000- to 100-hPa level. The left-hand term represents the MSE tendency, and the right-hand terms denote the horizontal and vertical advection, the sum of surface sensible and latent heat flux (Q_t), and the sum of vertically integrated longwave and shortwave radiation heating rate (Q_r), respectively.

In addition, under the weak temperature gradient approximation (Sobel et al. 2001), the water vapor dominates the MSE and plays a key role in regulating tropical intraseasonal convection (Adames and Maloney 2021). The formula of the moisture budget is written as follows:

$$\frac{\partial q}{\partial t} = -\mathbf{V} \cdot \nabla q - \omega \frac{\partial q}{\partial p} - \frac{Q_2}{L}, \tag{3}$$

where Q_2 is the apparent moisture sink, and L is the latent heat of condensation. The left-hand term represents the specific humidity tendency, and the right-hand terms denote the horizontal advection, vertical advection, and moisture changing rate due to condensational heating, respectively.

Figure 9 illustrates evolution of the regressed column vertically integrated MSE anomalies and averaged specific humidity anomalies in the lower troposphere (850–400 hPa) against Indian Ocean OLR anomalies at RTD8. The close association between MSE and specific humidity anomalies is clearly seen in both observations and all the three sets of experiments. Also, the evolution of these MSE and moisture anomalies is consistent with MJO convective signals in the observation and experiments (recall Fig. 7). In the observation, the eastward propagation of the maximum moisture (MSE) anomalies is closely associated with the eastward-propagating MJO convection (Fig. 9a). Also consistent with the standing MJO convection over the TIO in both the CTL and AMIP experiments, standing moisture (and MSE) anomalies are also discerned (Figs. 9b,c). In the CGCM experiment, maximum moisture (MSE) anomalies show gradual eastward migration along with the MJO convection, although these eastward-moving moisture (MSE) anomalies are less well organized as in the observations (Fig. 9d).

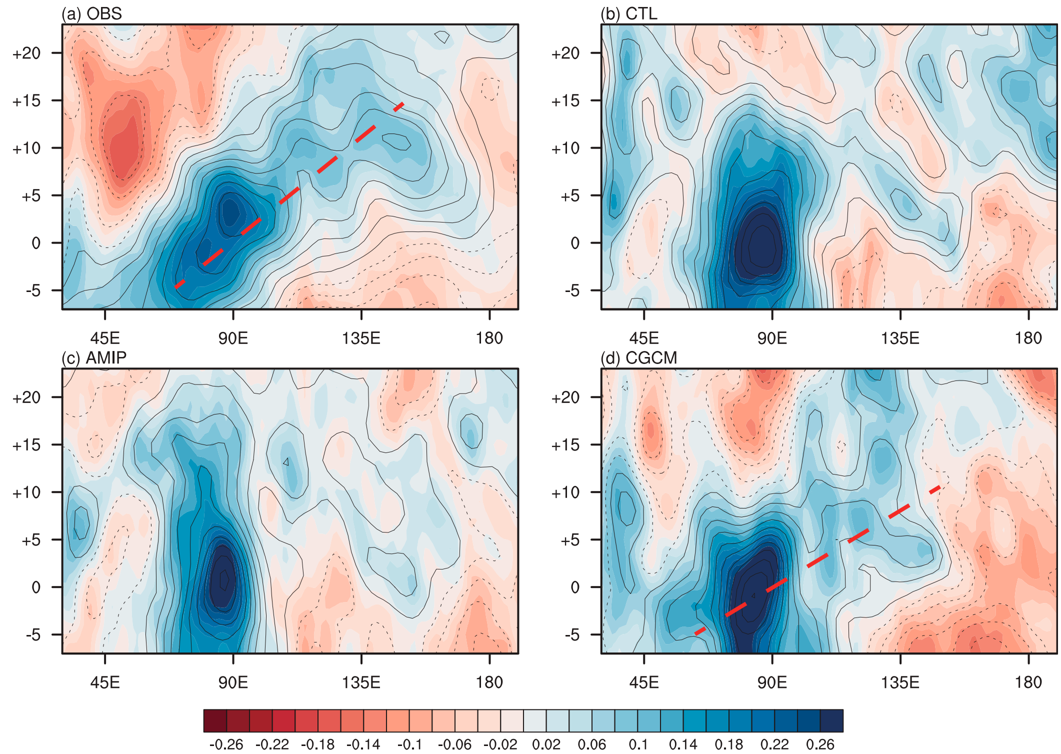

FIG. 9. Hovmöller diagram of the regressed intraseasonal anomalies of 1000–100-hPa mass-weighted column-integrated MSE (contour interval: 1×10^6 J m^{-2}) and 850–400-hPa vertically averaged specific humidity (shaded; g kg^{-1}) averaged between 10°N and 10°S (spatial smoothing is done by a nine-point running average) in (a) observations, (b) CTL, (c) AMIP, and (d) CGCM hindcasts. The *y* axis denotes the lag days from the reference time (i.e., the eighth day of each month). Red dashed lines denote the propagating trajectory of the center of the moisture (and MSE) anomalies in the observation and the CGCM.

These above results, therefore, suggest that the higher MJO prediction skill in the CGCM experiment can be attributed to better representation of moisture processes that promote MJO convection. A further diagnosis shows that the midtropospheric moisture anomaly maximum, corresponding to the MJO deep convective center, can propagate eastward to the MC region in the observation and CGCM hindcast from lag 0 to lag +10 (Figs. 10a,d,e,h). In contrast, this propagation is not successfully predicted in the CTL and AMIP experiments (Figs. 10b,c,f,g). One key factor that regulates this process may be a more distinct dipole pattern of the moisture tendency in the observation and CGCM, that is, moistening (drying) to the east (west) of MJO major convection (Figs. 10i–l), which is associated with the horizontal moisture advection modulated by the MJO circulation (Jiang 2017; Jiang et al. 2020b). However, deficiencies are also noted in the CGCM. For example, the propagation of the moisture anomalies is not well organized, and the moistening to the east of MJO convection is also weaker than that in the observation.

Figure 11 further displays vertical–longitudinal cross sections of anomalous circulation overlaid by the specific humidity anomalies, derived by lag-0 regressions of these fields onto the OLR anomalies over the EEIO. The enhanced moisture anomalies, with their maximum in the midtroposphere, are largely collocated with the MJO convection in both observations and three hindcast experiments (Figs. 11a–d). A notable difference in moisture anomalous patterns between the CGCM and two AGCM-only experiments is found in the planetary boundary layer (PBL) and lower troposphere to the east of MJO convection center. Consistent with the observations (Fig. 11a), positive moisture anomalies are detected in the boundary layer and the lower troposphere prior to this deep convection in the CGCM experiment (Fig. 11d), which tends to create an unstable stratification and moisture preconditions to promote the eastward propagation of MJO convection (e.g., Hsu and Li 2012; Hu et al. 2020). As a result, the vertical moisture anomalous patterns in both observations and CGCM display a vertical tilting structure, in agreement with a typical evolution from shallow/congestus clouds to deep clouds associated with the development of MJO convection (Benedict and Randall 2007). However, this shallow convection is largely missing in the CTL and AMIP experiments (Figs. 11b,c), which can be responsible for the weak eastward propagation of MJO convection in these two experiments.

Significant differences in the MJO zonal scale are also noted between the two AGCM-only and the CGCM hindcasts (Figs. 11b–d). While the strongest descending motion to the east of MJO convection is present to the east of 150°E in both observations and the CGCM experiment (Figs. 11a,d), it appears near 120°E in both the CTL and AMIP hindcasts (Figs. 11b,c), suggesting a smaller MJO zonal scale in the two

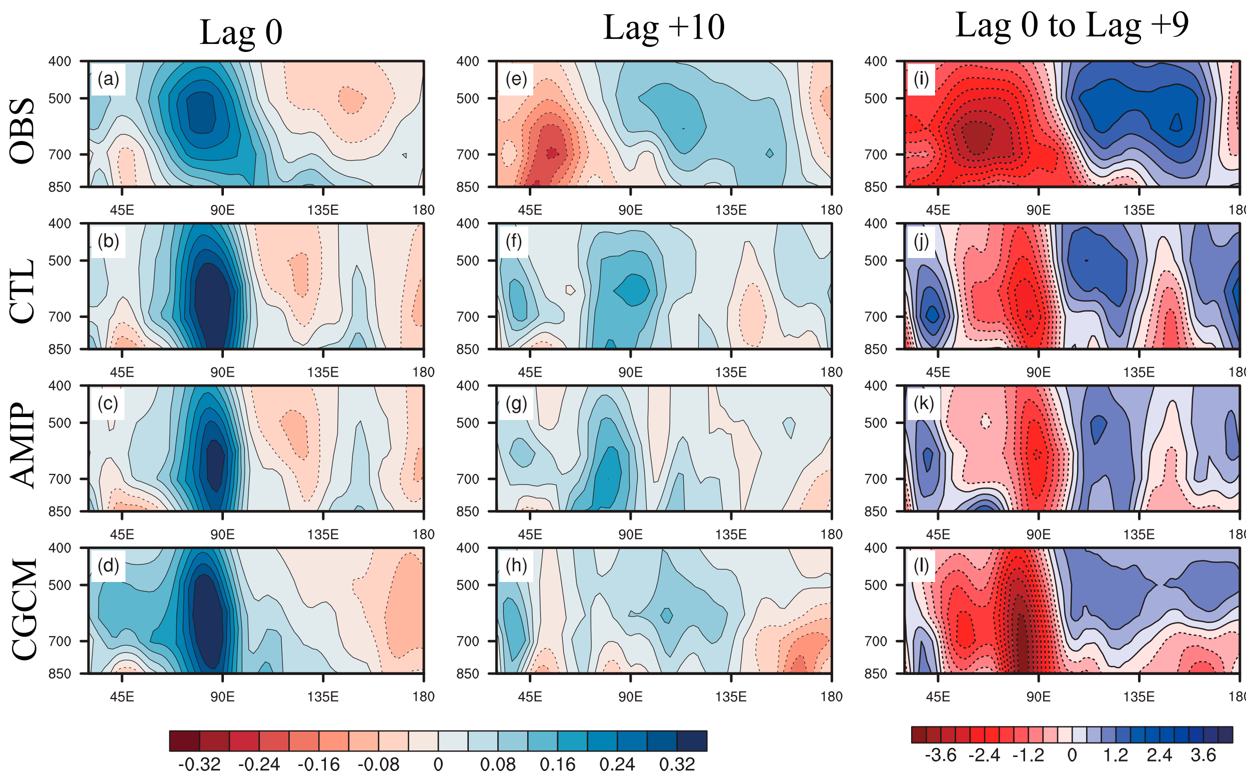

FIG. 10. The evolution of moisture in the free troposphere (850–400 hPa). Vertical–longitude cross section of the regressed specific humidity anomalies (units g kg^{-1}) averaged over 10°N–10°S (spatial smoothing is done by a nine-point running average) at (left) lag 0 and (center) lag +10, and (right) the regressed specific humidity tendencies (unit 10^{-10} kg kg^{-1} s^{-1}) averaged from lag 0 to lag +9.

AGCM experiments. Meanwhile, relatively stronger Kelvin wave responses to the east of MJO convection in the lower troposphere are also found in the CGCM experiment (Fig. 11d) than those in the two AGCM experiments (Figs. 11b,c), which is further illustrated by Fig. 11e.

Recent studies have suggested that the zonal scale of MJO circulation is closely associated with MJO propagation (Wang et al. 2019; Wei and Ren 2019; Chen and Wang 2020). A large MJO zonal scale along with extended and strong Kelvin wave responses will be conducive to organized moistening to the east of MJO convection through horizontal moisture advection (Lyu et al. 2021) and boundary layer moisture convergence, possibly through an enhanced shallow convection and circulation feedback (Wang and Lee 2017; Wang et al. 2019; Chen and Wang 2020), therefore favors the MJO eastward propagation.

c. *Convection–SST feedback*

In general, 1) a better prediction of low-level moistening (shallow convection) preceding MJO major convection and 2) free-tropospheric east–west asymmetry of the moisture tendency related to the MJO zonal scale jointly contribute to an improved prediction of the MJO propagation in the CGCM. Although the key factor determining these MJO structures remains unclear, the above results suggest a possible contribution from the air–sea interaction. To further investigate the role of atmosphere–ocean coupling, lag-0 regressed equator-averaged (10°N–10°S) SST anomalies against the EEIO OLR anomaly on RTD8 are also shown on the bottom of each panel in Fig. 11. Note that SSTs prescribed in the CTL experiment are climatological values, and therefore this analysis was not applied to the CTL hindcasts.

An east–west asymmetry of the SST anomalies relative to the MJO convection is clearly seen in the observations (Fig. 11a), i.e., warm (cold) anomalies are present over the MC (TIO) region, as a result of a combination of radiative effect and wind–evaporation feedback (DeMott et al. 2015). In association with the vertical tilting structure of cloudiness, the solar radiation is reduced in the MJO convection center and its west flank but enhanced ahead of the convection. In addition, the anomalous easterly (westerly) winds produced by convective heating can reduce (enhance) evaporation to the east (west) of MJO convection over the Indo-Pacific warm pool sector. Both the reduced evaporation and increased solar radiation favor increasing SST, and vice versa.

However, this observed SST anomalous pattern is absent in the AMIP experiment (Fig. 11c), due to the lack of atmospheric feedback to the ocean in this experiment. Instead, with a two-way coupling between the atmosphere and ocean components, the CGCM can generate more realistic SST responses to the MJO (Fig. 11d). This MJO-induced SST

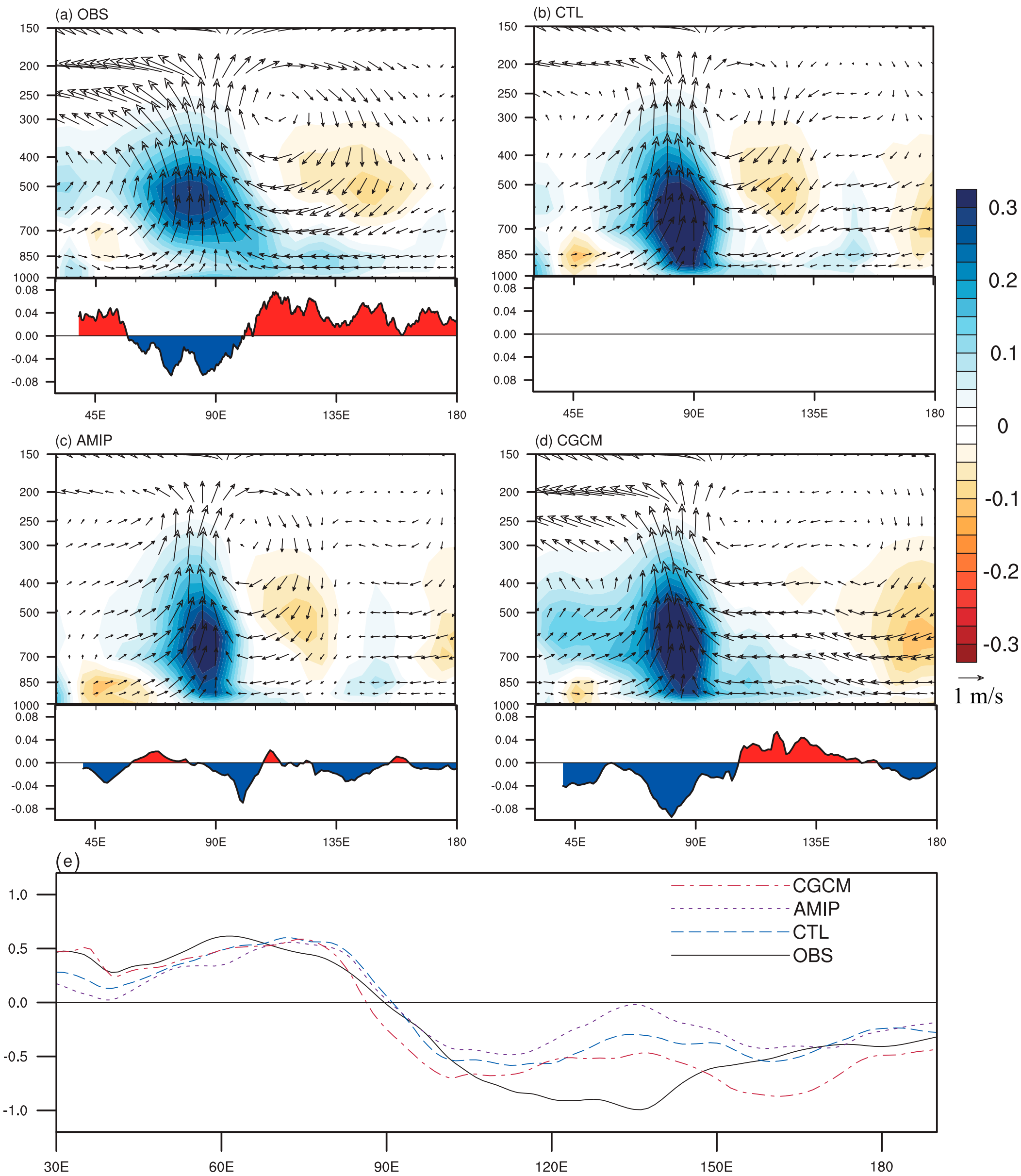

FIG. 11. Vertical–longitude cross section of lag-0 regressed specific humidity anomalies (shaded; unit: g kg^{-1}), anomalous zonal and vertical winds (vectors; m s^{-1} for zonal wind velocity and 0.01 Pa s^{-1} for vertical velocity) averaged over 10°N–10°S in the (a) observations, (b) CTL, (c) AMIP, and (d) CGCM hindcasts. Lag-0 regressed SST anomalies (unit: °C) averaged over 10°N–10°S are attached at the bottom of each panel. (e) Lag-0 regressed U850 anomalies along the equator (10°N–10°S average) based on the observation (black solid line), CTL (blue long-dashed line), AMIP (purple short-dashed line), and CGCM (red dot–dashed line) hindcasts.

fluctuation in turn can feed back to the atmosphere (DeMott et al. 2015). For example, the warm SST anomalies to the east of MJO major convection can help organize the shallow convection and Kelvin wave by enhancing the PBL convergence and latent heat flux (e.g., Marshall et al. 2008; Hsu and Li 2012; DeMott et al. 2019). The warmer SST to the east of MJO convection could also help to sustain a larger zonal-scale in MJO circulation as indicated by several recent studies (Wei and Ren 2019; Chen and Wang 2020; Lyu et al. 2021) and is therefore conducive to the MJO propagation as previously discussed, although the detailed processes determining the MJO zonal scale need to be further investigated (e.g., Lyu et al. 2021). Also, the cold SST response to the west can facilitate the demise of convection. All the feedbacks will be conducive to the eastward propagation of the MJO. In contrast, the lack of this air–sea coupling could be responsible for weak moisture

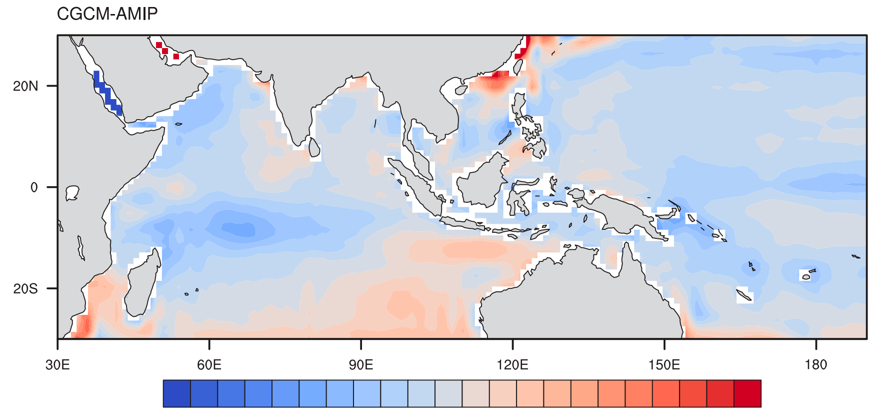

FIG. 12. Difference of climatological mean SST of November–April between the 1-month CGCM prediction and the AMIP experiment during 1984–2008.

preconditioning process and thus weak MJO propagation in the two AGCM-only hindcasts.

6. Summary and discussion

In this study we examined the importance of air–sea coupling in predicting the MJO. By comparing the MJO forecast skill in three sets of hindcast experiments conducted by AGCM-only models and atmosphere–ocean coupled model, respectively, we find that the coupled model shows better forecasts than the AGCM, supporting previous studies that air–sea interactions can play an important role for the MJO.

Associated with the seasonality in propagation and intensity of the MJO (e.g., Madden 1986; Wang and Rui 1990), different MJO skill is found during boreal winter and summer (e.g., Wang et al. 2014), with a higher skill for MJO events during boreal winter than in summer. Note that the seasonal skill comparison is based on the RMM indices, which might be unrepresentative to the poleward and westward propagating components in boreal summer. Thus, our study is mainly focused on the winter skill intercomparison among the three hindcast experiments. We find that the advantage of atmosphere–ocean coupled model over the AGCM in forecasting the RMM indices is remarkable during boreal winter (recall Fig. 5a); useful skill (ACC > 0.5) is found out to about 3 weeks lead in the coupled model experiment, which is about 1 week longer than those in the AGCM-only experiments.

In addition to the improved prediction of the RMM indices, the coupled model can realistically predict the temporospatial evolution of the MJO at longer lead times. This result can be explained by several mechanisms under different theoretical frameworks. From the moisture mode perspective (Sobel and Maloney 2012; Adames and Maloney 2021), the improvement in MJO prediction by air–sea coupling can be attributed to the improved forecast of moisture evolutions. The CGCM can reproduce a more realistic east–west dipole of the midtropospheric moisture tendency, which likely arises from a better prediction of the zonal scale of MJO circulation. In addition, the low-level moistening ahead of the MJO convection, which corresponds to the shallow convection and precondition for MJO deep convection (Hsu and Li 2012), is better predicted in the CGCM. Moreover, stronger Kelvin wave responses to the east of MJO convection are also found in the CGCM, which could also help to enhance MJO eastward propagations based on the ‘‘trio-interaction’’ theory (Wang et al. 2016; Wang and Lee 2017).

Further analysis reveals that the better MJO prediction skill in the CGCM could be also contributed by the improved representation of high-frequency SST fluctuations related to the MJO with warm (cold) SST anomalies to the east (west) of MJO convection, through the aforementioned convection–SST feedback processes. The SST feedbacks are missing in the AGCM experiments due to the lack of air–sea coupling, as previously reported (Kim et al. 2010).

Previous studies argued that the comparison between the AGCM and CGCM conflates the influences of mean state and atmosphere–ocean coupling (e.g., Klingaman and DeMott 2020), and the coupling with the ocean could induce a different mean state. The climatological SSTs of the CGCM 1-month lead predictions show a weak cold bias in the TIO and WP (Fig. 12), which could not favor the convection. Therefore, it does not appear that the slightly different SST climatology in the CGCM may be responsible for the improved prediction of the MJO. In addition, we focus on the moisture processes over the eastern TIO, MC, and WP where the SST biases in the CGCM are quite small (Fig. 12), so the difference of the climatological SSTs among the hindcast experiments does not appear to have much impact on our general conclusions.

In addition, previous studies also suggested that models' systematic dry bias in simulating the climatological mean moisture over the MC–WP sector can be an important factor that restricts models' ability to simulate MJO propagation (e.g., Gonzalez and Jiang 2017; Jiang 2017). The climatological mean moisture in the three hindcast experiments also shows noticeable biases (Fig. 13), which may limit the forecast skill of the MJO in the models. Interestingly, compared to the AGCM-only hindcasts, the climatological mean moisture in the CGCM shows no significant improvement. Therefore, the improved MJO prediction in the

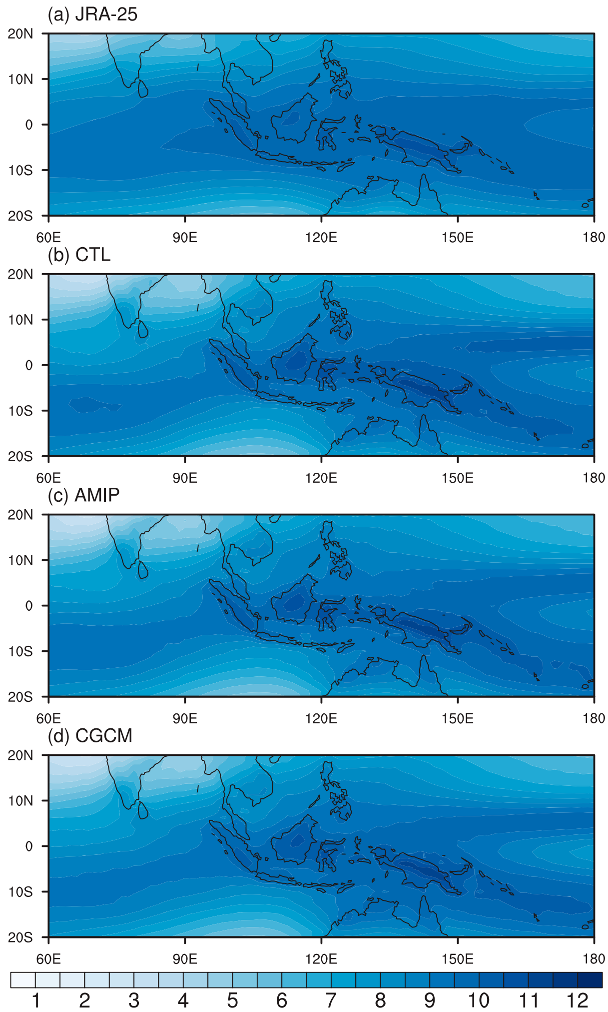

FIG. 13. The climatological mean specific humidity (units: g kg^{-1}) of November–April averaged over lower troposphere (925–600 hPa) based on (a) JRA-25, (b) the CTL, (c) AMIP, and (d) CGCM hindcasts. The moisture mean states of the model hindcasts are calculated based on the forecasts at 2-week lead.

CGCM experiment may be attributed to the better predicted MJO circulation (recall Fig. 11). However, large discrepancy exists between the MJO prediction skill in our coupled model prediction system and world-leading forecast systems such as ECMWF and GFDL (e.g., Xiang et al. 2015; Kim et al. 2018). This demands future efforts to improve our forecast system, including better initialization schemes and advanced model physics schemes, etc. On top of that, a multimember and multimodel ensemble forecast system based on fully coupled atmosphere–ocean models is expected to be helpful for reducing the influences of uncertainties in initial conditions and model errors and making probabilistic forecasts.

Acknowledgments. This work is supported by National Natural Science Foundation of China (Grants 42030605 and 42088101) and National Key R&D Program of China (Grant 2020YFA0608004). The numerical calculations in this study were conducted in the High Performance Computing Center of Nanjing University of Information Science and Technology. We thank three anonymous reviewers for their comments that greatly helped improve the original manuscript.

REFERENCES

Adames, Á. F., and E. D. Maloney, 2021: Moisture mode theory's contribution to advances in our understanding of the Madden–Julian Oscillation and other tropical disturbances. *Curr. Climate Change Rep.*, **7**, 72–85, https://doi.org/10.1007/s40641-021-00172-4.

Benedict, J. J., and D. A. Randall, 2007: Observed characteristics of the MJO relative to maximum rainfall. *J. Atmos. Sci.*, **64**, 2332–2354, https://doi.org/10.1175/JAS3968.1.

Cassou, C., 2008: Intraseasonal interaction between the Madden–Julian Oscillation and the North Atlantic Oscillation. *Nature*, **455**, 523–527, https://doi.org/10.1038/nature07286.

Chen, G., and B. Wang, 2020: Circulation factors determining the propagation speed of the Madden–Julian oscillation. *J. Climate*, **33**, 3367–3380, https://doi.org/10.1175/JCLI-D-19-0661.1.

DeMott, C. A., N. P. Klingaman, and S. J. Woolnough, 2015: Atmosphere–ocean coupled processes in the Madden–Julian oscillation. *Rev. Geophys.*, **53**, 1099–1154, https://doi.org/10.1002/2014RG000478.

——, J. J. Benedict, N. P. Klingaman, S. J. Woolnough, and D. A. Randall, 2016: Diagnosing ocean feedbacks to the MJO: SST-modulated surface fluxes and the moist static energy budget. *J. Geophys. Res. Atmos.*, **121**, 8350–8373, https://doi.org/10.1002/2016JD025098.

——, N. P. Klingaman, W.-L. Tseng, M. A. Burt, Y. Gao, and D. A. Randall, 2019: The convection connection: How ocean feedbacks affect tropical mean moisture and MJO propagation. *J. Geophys. Res. Atmos.*, **124**, 11 910–11 931, https://doi.org/10.1029/2019JD031015.

Fu, X., B. Wang, J.-Y. Lee, W. Wang, and L. Gao, 2011: Sensitivity of dynamical intraseasonal prediction skills to different initial conditions. *Mon. Wea. Rev.*, **139**, 2572–2592, https://doi.org/10.1175/2011MWR3584.1.

——, J.-Y. Lee, P.-C. Hsu, H. Taniguchi, B. Wang, W. Wang, and S. Weaver, 2013: Multi-model MJO forecasting during DYNAMO/CINDY period. *Climate Dyn.*, **41**, 1067–1081, https://doi.org/10.1007/s00382-013-1859-9.

——, W. Wang, J.-Y. Lee, B. Wang, K. Kikuchi, J. Xu, J. Li, and S. Weaver, 2015: Distinctive roles of air–sea coupling on different MJO events: A new perspective revealed from the DYNAMO/CINDY field campaign. *Mon. Wea. Rev.*, **143**, 794–812, https://doi.org/10.1175/MWR-D-14-00221.1.

Gill, A. E., 1980: Some simple solutions for heat-induced tropical circulation. *Quart. J. Roy. Meteor. Soc.*, **106**, 447–462, https://doi.org/10.1002/qj.49710644905.

Gonzalez, A. O., and X. Jiang, 2017: Winter mean lower tropospheric moisture over the Maritime Continent as a climate model diagnostic metric for the propagation of the Madden–Julian oscillation. *Geophys. Res. Lett.*, **44**, 2588–2596, https://doi.org/10.1002/2016GL072430.

Gottschalck, J., and Coauthors, 2010: A framework for assessing operational Madden–Julian oscillation forecasts. *Bull. Amer. Meteor. Soc.*, **91**, 1247–1258, https://doi.org/10.1175/2010BAMS2816.1.

Green, B. W., S. Sun, R. Bleck, S. G. Benjamin, and G. A. Grell, 2017: Evaluation of MJO predictive skill in multiphysics and multimodel global ensembles. *Mon. Wea. Rev.*, **145**, 2555–2574, https://doi.org/10.1175/MWR-D-16-0419.1.

He, J., J. Wu, and J. Luo, 2020: Introduction to climate forecast system version 1.0 of Nanjing University of Information Science and Technology (in Chinese). *Trans. Atmos. Sci.*, **43**, 128–143.

Hsu, P.-C., and T. Li, 2012: Role of the boundary layer moisture asymmetry in causing the eastward propagation of the Madden–Julian oscillation. *J. Climate*, **25**, 4914–4931, https://doi.org/10.1175/JCLI-D-11-00310.1.

Hu, F., T. Li, J. Gao, and L. Hao, 2020: Reexamining the moisture mode theories of the Madden–Julian oscillation based on observational analyses. *J. Climate*, **34**, 839–853, https://doi.org/10.1175/JCLI-D-20-0441.1.

Jeuken, A. B. M., P. C. Siegmund, L. C. Heijboer, J. Feichter, and L. Bengtsson, 1996: On the potential of assimilating meteorological analyses in a global climate model for the purpose of model validation. *J. Geophys. Res.*, **101**, 16 939–16 950, https://doi.org/10.1029/96JD01218.

Jiang, X., 2017: Key processes for the eastward propagation of the Madden–Julian Oscillation based on multimodel simulations. *J. Geophys. Res. Atmos.*, **122**, 755–770, https://doi.org/10.1002/2016JD025955.

——, T. Li, and B. Wang, 2004: Structures and mechanisms of the northward propagating boreal summer intraseasonal oscillation. *J. Climate*, **17**, 1022–1039, https://doi.org/10.1175/1520-0442(2004)017<1022:SAMOTN>2.0.CO;2.

——, Á. F. Adames, M. Zhao, D. Waliser, and E. Maloney, 2018: A unified moisture mode framework for seasonality of the Madden–Julian oscillation. *J. Climate*, **31**, 4215–4224, https://doi.org/10.1175/JCLI-D-17-0671.1.

——, and Coauthors, 2020a: Fifty years of research on the Madden–Julian oscillation: Recent progress, challenges, and perspectives. *J. Geophys. Res. Atmos.*, **125**, e2019JD030911, https://doi.org/10.1029/2019JD030911.

——, E. Maloney, and H. Su, 2020b: Large-scale controls of propagation of the Madden–Julian Oscillation. *npj Climate Atmos. Sci.*, **3**, 29, https://doi.org/10.1038/s41612-020-00134-x.

Kim, H.-M., 2017: The impact of the mean moisture bias on the key physics of MJO propagation in the ECMWF reforecast. *J. Geophys. Res. Atmos.*, **122**, 7772–7784, https://doi.org/10.1002/2017JD027005.

——, C. D. Hoyos, P. J. Webster, and I.-S. Kang, 2008: Sensitivity of MJO simulation and predictability to sea surface temperature variability. *J. Climate*, **21**, 5304–5317, https://doi.org/10.1175/2008JCLI2078.1.

——, ——, ——, and ——, 2010: Ocean–atmosphere coupling and the boreal winter MJO. *Climate Dyn.*, **35**, 771–784, https://doi.org/10.1007/s00382-009-0612-x.

——, P. J. Webster, V. E. Toma, and D. Kim, 2014: Predictability and prediction skill of the MJO in two operational forecasting systems. *J. Climate*, **27**, 5364–5378, https://doi.org/10.1175/JCLI-D-13-00480.1.

——, F. Vitart, and D. E. Waliser, 2018: Prediction of the Madden–Julian oscillation: A review. *J. Climate*, **31**, 9425–9443, https://doi.org/10.1175/JCLI-D-18-0210.1.

——, J. H. Richter, and Z. Martin, 2019: Insignificant QBO–MJO prediction skill relationship in the SubX and S2S subseasonal reforecasts. *J. Geophys. Res. Atmos.*, **124**, 12 655–12 666, https://doi.org/10.1029/2019JD031416.

Klingaman, N. P., and S. J. Woolnough, 2014: The role of air–sea coupling in the simulation of the Madden–Julian oscillation in the Hadley Centre model. *Quart. J. Roy. Meteor. Soc.*, **140**, 2272–2286, https://doi.org/10.1002/qj.2295.

——, and C. A. DeMott, 2020: Mean state biases and interannual variability affect perceived sensitivities of the Madden–Julian oscillation to air–sea coupling. *J. Adv. Model. Earth Syst.*, **12**, e2019MS001799, https://doi.org/10.1029/2019MS001799.

Lawrence, D. M., and P. J. Webster, 2002: The boreal summer intraseasonal oscillation: Relationship between northward and eastward movement of convection. *J. Atmos. Sci.*, **59**, 1593–1606, https://doi.org/10.1175/1520-0469(2002)059<1593:TBSIOR>2.0.CO;2.

Liebmann, B., and C. A. Smith, 1996: Description of a complete (interpolated) outgoing longwave radiation dataset. *Bull. Amer. Meteor. Soc.*, **77**, 1275–1277, https://doi.org/10.1175/1520-0477-77.6.1274.

Lim, Y., S.-W. Son, and D. Kim, 2018: MJO prediction skill of the subseasonal-to-seasonal prediction models. *J. Climate*, **31**, 4075–4094, https://doi.org/10.1175/JCLI-D-17-0545.1.

——, ——, A. G. Marshall, H. H. Hendon, and K.-H. Seo, 2019: Influence of the QBO on MJO prediction skill in the subseasonal-to-seasonal prediction models. *Climate Dyn.*, **53**, 1681–1695, https://doi.org/10.1007/s00382-019-04719-y.

Lin, H., G. Brunet, and J. Derome, 2008: Forecast skill of the Madden–Julian oscillation in two Canadian atmospheric models. *Mon. Wea. Rev.*, **136**, 4130–4149, https://doi.org/10.1175/2008MWR2459.1.

Liu, F., and B. Wang, 2013: An air–sea coupled skeleton model for the Madden–Julian oscillation. *J. Atmos. Sci.*, **70**, 3147–3156, https://doi.org/10.1175/JAS-D-12-0348.1.

Liu, X., and Coauthors, 2017: MJO prediction using the subseasonal to seasonal forecast model of Beijing Climate Center. *Climate Dyn.*, **48**, 3283–3307, https://doi.org/10.1007/s00382-016-3264-7.

Luo, J.-J., S. Masson, S. K. Behera, P. Delecluse, S. Gualdi, A. Navarra, and T. Yamagata, 2003: South Pacific origin of the decadal ENSO-like variation as simulated by a coupled GCM. *Geophys. Res. Lett.*, **30**, 2250, https://doi.org/10.1029/2003GL018649.

——, ——, ——, S. Shingu, and T. Yamagata, 2005a: Seasonal climate predictability in a coupled OAGCM using a different approach for ensemble forecasts. *J. Climate*, **18**, 4474–4497, https://doi.org/10.1175/JCLI3526.1.

——, ——, E. Roeckner, G. Madec, and T. Yamagata, 2005b: Reducing climatology bias in an ocean–atmosphere CGCM with improved coupling physics. *J. Climate*, **18**, 2344–2360, https://doi.org/10.1175/JCLI3404.1.

——, ——, S. K. Behera, and T. Yamagata, 2007: Experimental forecasts of the Indian Ocean dipole using a coupled OAGCM. *J. Climate*, **20**, 2178–2190, https://doi.org/10.1175/JCLI4132.1.

——, ——, ——, and ——, 2008a: Extended ENSO predictions using a fully coupled ocean–atmosphere model. *J. Climate*, **21**, 84–93, https://doi.org/10.1175/2007JCLI1412.1.

——, S. K. Behera, Y. Masumoto, H. Sakuma, and T. Yamagata, 2008b: Successful prediction of the consecutive IOD in 2006 and 2007. *Geophys. Res. Lett.*, **35**, L14S02, https://doi.org/10.1029/2007GL032793.

Lyu, M., X. Jiang, Z. Wu, D. Kim, and Á. F. Adames, 2021: Zonal-scale of the Madden–Julian Oscillation and its propagation speed on the interannual time-scale. *Geophys. Res. Lett.*, **48**, e2020GL091239, https://doi.org/10.1029/2020GL091239.

Madden, R. A., 1986: Seasonal variations of the 40–50 day oscillation in the tropics. *J. Atmos. Sci.*, **43**, 3138–3158, https://doi.org/10.1175/1520-0469(1986)043<3138:SVOTDO>2.0.CO;2.

——, and P. R. Julian, 1971: Detection of a 40–50 day oscillation in the zonal wind in the tropical Pacific. *J. Atmos. Sci.*, **28**, 702–708, https://doi.org/10.1175/1520-0469(1971)028<0702:DOADOI>2.0.CO;2.

——, and ——, 1972: Description of global-scale circulation cells in the tropics with a 40–50 day period. *J. Atmos. Sci.*, **29**, 1109–1123, https://doi.org/10.1175/1520-0469(1972)029<1109:DOGSCC>2.0.CO;2.

Madec, G., P. Delecluse, M. Imbard, and C. Levy, 1998: OPA 8.1 ocean general circulation model reference manual. LODYC/IPSL Tech. Note 11, 91 pp., https://www.nemo-ocean.eu/wp-content/uploads/Doc_OPA8.1.pdf.

Maloney, E. D., 2009: The moist static energy budget of a composite tropical intraseasonal oscillation in a climate model. *J. Climate*, **22**, 711–729, https://doi.org/10.1175/2008JCLI2542.1.

Marshall, A. G., O. Alves, and H. H. Hendon, 2008: An enhanced moisture convergence–evaporation feedback mechanism for MJO air–sea interaction. *J. Atmos. Sci.*, **65**, 970–986, https://doi.org/10.1175/2007JAS2313.1.

——, H. H. Hendon, S.-W. Son, and Y. Lim, 2017: Impact of the quasi-biennial oscillation on predictability of the Madden–Julian oscillation. *Climate Dyn.*, **49**, 1365–1377, https://doi.org/10.1007/s00382-016-3392-0.

Matsuno, T., 1966: Quasi-geostrophic motions in the equatorial area. *J. Meteor. Soc. Japan*, **44**, 25–43, https://doi.org/10.2151/jmsj1965.44.1_25.

Merryfield, W. J., and Coauthors, 2020: Current and emerging developments in subseasonal to decadal prediction. *Bull. Amer. Meteor. Soc.*, **101** (6), E869–E896, https://doi.org/10.1175/BAMS-D-19-0037.1.

Morcrette, J.-J., L. Smith, and Y. Fouquart, 1986: Pressure and temperature dependence of the absorption in longwave radiation parameterizations. *Beitr. Phys. Atmos.*, **59**, 455–469.

Neena, J. M., J. Y. Lee, D. Waliser, B. Wang, and X. Jiang, 2014: Predictability of the Madden–Julian oscillation in the Intraseasonal Variability Hindcast Experiment (ISVHE). *J. Climate*, **27**, 4531–4543, https://doi.org/10.1175/JCLI-D-13-00624.1.

Onogi, K., and Coauthors, 2007: The JRA-25 reanalysis. *J. Meteor. Soc. Japan*, **85**, 369–432, https://doi.org/10.2151/jmsj.85.369.

Palmer, T. N., F. J. Doblas-Reyes, A. Weisheimer, and M. J. Rodwell, 2008: Toward seamless prediction: Calibration of climate change projections using seasonal forecasts. *Bull. Amer. Meteor. Soc.*, **89**, 459–470, https://doi.org/10.1175/BAMS-89-4-459.

Pegion, K., and P. D. Sardeshmukh, 2011: Prospects for improving subseasonal predictions. *Mon. Wea. Rev.*, **139**, 3648–3666, https://doi.org/10.1175/MWR-D-11-00004.1.

Rashid, H. A., H. H. Hendon, M. C. Wheeler, and O. Alves, 2011: Prediction of the Madden–Julian oscillation with the POAMA dynamical prediction system. *Climate Dyn.*, **36**, 649–661, https://doi.org/10.1007/s00382-010-0754-x.

Reynolds, R. W., N. A. Rayner, T. M. Smith, D. C. Stokes, and W. Wang, 2002: An improved in situ and satellite SST analysis for climate. *J. Climate*, **15**, 1609–1625, https://doi.org/10.1175/1520-0442(2002)015<1609:AIISAS>2.0.CO;2.

——, T. M. Smith, C. Liu, D. B. Chelton, K. S. Casey, and M. G. Schlax, 2007: Daily high-resolution-blended analyses for sea surface temperature. *J. Climate*, **20**, 5473–5496, https://doi.org/10.1175/2007JCLI1824.1.

Roeckner, E., and Coauthors, 1996: The atmospheric general circulation model ECHAM-4: Model description and simulation of present-day climate. Max-Planck-Institut für Meteorologie Rep. 218, Hamburg, Germany, 90 pp.

Seo, K.-H., W. Wang, J. Gottschalck, Q. Zhang, J.-K. E. Schemm, W. R. Higgins, and A. Kumar, 2009: Evaluation of MJO forecast skill from several statistical and dynamical forecast models. *J. Climate*, **22**, 2372–2388, https://doi.org/10.1175/2008JCLI2421.1.

Shelly, A., P. Xavier, D. Copsey, T. Johns, J. M. Rodríguez, S. Milton, and N. Klingaman, 2014: Coupled versus uncoupled hindcast simulations of the Madden–Julian Oscillation in the year of tropical convection. *Geophys. Res. Lett.*, **41**, 5670–5677, https://doi.org/10.1002/2013GL059062.

Sobel, A. H., and E. Maloney, 2012: An idealized semi-empirical framework for modeling the Madden–Julian oscillation. *J. Atmos. Sci.*, **69**, 1691–1705, https://doi.org/10.1175/JAS-D-11-0118.1.

——, J. Nilsson, and L. M. Polvani, 2001: The weak temperature gradient approximation and balanced tropical moisture waves. *J. Atmos. Sci.*, **58**, 3650–3665, https://doi.org/10.1175/1520-0469(2001)058<3650:TWTGAA>2.0.CO;2.

Son, S.-W., Y. Lim, C. Yoo, H. H. Hendon, and J. Kim, 2017: Stratospheric control of the Madden–Julian oscillation. *J. Climate*, **30**, 1909–1922, https://doi.org/10.1175/JCLI-D-16-0620.1.

Stan, C., D. M. Straus, J. S. Frederiksen, H. Lin, E. D. Maloney, and C. Schumacher, 2017: Review of tropical–extratropical teleconnections on intraseasonal time scales. *Rev. Geophys.*, **55**, 902–937, https://doi.org/10.1002/2016RG000538.

Tiedtke, M., 1989: A comprehensive mass flux scheme for cumulus parameterization in large-scale models. *Mon. Wea. Rev.*, **117**, 1779–1800, https://doi.org/10.1175/1520-0493(1989)117<1779:ACMFSF>2.0.CO;2.

Valcke, S., L. Terray, and A. Piacentini, 2000: The OASIS coupler user guide version 2.4. CERFACE Tech. Rep. TR/CGMC/00-10, 85 pp.

Vitart, F., 2017: Madden–Julian oscillation prediction and teleconnections in the S2S database. *Quart. J. Roy. Meteor. Soc.*, **143**, 2210–2220, https://doi.org/10.1002/qj.3079.

——, and Coauthors, 2017: The Subseasonal to Seasonal (S2S) prediction project database. *Bull. Amer. Meteor. Soc.*, **98**, 163–173, https://doi.org/10.1175/BAMS-D-16-0017.1.

Waliser, D. E., K. M. Lau, W. Stern, and C. Jones, 2003: Potential predictability of the Madden–Julian oscillation. *Bull. Amer. Meteor. Soc.*, **84**, 33–50, https://doi.org/10.1175/BAMS-84-1-33.

Wang, B., and H. Rui, 1990: Synoptic climatology of transient tropical intraseasonal convection anomalies: 1975–1985. *Meteor. Atmos. Phys.*, **44**, 43–61, https://doi.org/10.1007/BF01026810.

——, and X. Xie, 1996: A model for the boreal summer intraseasonal oscillation. *J. Atmos. Sci.*, **54**, 72–86, https://doi.org/10.1175/1520-0469(1997)054<0072:AMFTBS>2.0.CO;2.

——, and ——, 1998: Coupled modes of the warm pool climate system. Part I: The role of air–sea interaction in maintaining Madden–Julian oscillation. *J. Climate*, **11**, 2116–2135, https://doi.org/10.1175/1520-0442(1998)011<2116:CMOTWP>2.0.CO;2.

——, and S.-S. Lee, 2017: MJO propagation shaped by zonal asymmetric structures: Results from 24 GCM simulations. *J. Climate*, **30**, 7933–7952, https://doi.org/10.1175/JCLI-D-16-0873.1.

——, F. Liu, and G. Chen, 2016: A trio-interaction theory for Madden–Julian oscillation. *Geosci. Lett.*, **3**, 34, https://doi.org/10.1186/s40562-016-0066-z.

——, G. Chen, and F. Liu, 2019: Diversity of the Madden–Julian Oscillation. *Sci. Adv.*, **5**, eaax0220, https://doi.org/10.1126/sciadv.aax0220.

Wang, L., T. Li, L. Chen, S. K. Behera, and T. Nasuno, 2017a: Modulation of the MJO intensity over the equatorial western

Pacific by two types of El Niño. *Climate Dyn.*, **51**, 687–700, https://doi.org/10.1007/s00382-017-3949-6.

——, ——, E. Maloney, and B. Wang, 2017b: Fundamental causes of propagating and nonpropagating MJOs in MJOTF/GASS models. *J. Climate*, **30**, 3743–3769, https://doi.org/10.1175/JCLI-D-16-0765.1.

Wang, W., M.-P. Hung, S. J. Weaver, A. Kumar, and X. Fu, 2014: MJO prediction in the NCEP Climate Forecast System version 2. *Climate Dyn.*, **42**, 2509–2520, https://doi.org/10.1007/s00382-013-1806-9.

Wei, Y., and H.-L. Ren, 2019: Modulation of ENSO on fast and slow MJO modes during boreal winter. *J. Climate*, **32**, 7483–7506, https://doi.org/10.1175/JCLI-D-19-0013.1.

Wheeler, M. C., and H. H. Hendon, 2004: An all-season real-time multivariate MJO Index: Development of an index for monitoring and prediction. *Mon. Wea. Rev.*, **132**, 1917–1932, https://doi.org/10.1175/1520-0493(2004)132<1917:AARMMI>2.0.CO;2.

Woolnough, S. J., F. Vitart, and M. A. Balmaseda, 2007: The role of the ocean in the Madden–Julian Oscillation: Implications for MJO prediction. *Quart. J. Roy. Meteor. Soc.*, **133**, 117–128, https://doi.org/10.1002/qj.4.

Wu, J., H. L. Ren, B. Lu, P. Zhang, C. Zhao, and X. Liu, 2020: Effects of moisture initialization on MJO and its teleconnection prediction in BCC subseasonal coupled model. *J. Geophys. Res. Atmos.*, **125**, e2019JD031537, https://doi.org/10.1029/2019JD031537.

Xiang, B., M. Zhao, X. Jiang, S.-J. Lin, T. Li, X. Fu, and G. Vecchi, 2015: The 3–4-week MJO prediction skill in a GFDL coupled model. *J. Climate*, **28**, 5351–5364, https://doi.org/10.1175/JCLI-D-15-0102.1.

Zhang, C., 2005: Madden–Julian Oscillation. *Rev. Geophys.*, **43**, RG2003, https://doi.org/10.1029/2004RG000158.

——, 2013: Madden–Julian oscillation: Bridging weather and climate. *Bull. Amer. Meteor. Soc.*, **94**, 1849–1870, https://doi.org/10.1175/BAMS-D-12-00026.1.

——, Á. F. Adames, B. Khouider, B. Wang, and D. Yang, 2020: Four theories of the Madden–Julian Oscillation. *Rev. Geophys*, **58**, e2019RG000685, https://doi.org/10.1029/2019RG000685.